RESEARCH PAPER

A tomographic imagery segmentation methodology for three-phase geomaterials based on simultaneous region growing

**Mir Amid Hashemi · Ghonwa Khaddour ·
Bertrand François · Thierry J. Massart ·
Simon Salager**

Abstract X-ray computed tomography is a powerful non-destructive technique used in many domains to obtain the three-dimensional representation of objects, starting from the reconstitution of two-dimensional images of radiographic scanning. This technique is now able to analyze objects within a few micron resolutions. Consequently, X-ray microcomputed tomography opens perspectives for the analysis of the fabric of multiphase geomaterials such as soils, concretes, rocks and ceramics. To be able to characterize the spatial distribution of the different phases in such complex and disordered materials, automated phase recognition has to be implemented through image segmentation. A crucial difficulty in segmenting images lies in the presence of noise in the obtained tomographic representation, making it difficult to assign a specific phase to each voxel of the image. In the present study, simultaneous region growing is used to reconstitute the three-dimensional segmented image of granular materials. First, based on a set of expected phases in the image, regions where specific phases are sure to be present are identified, leaving uncertain regions of the image unidentified. Subsequently, the identified regions are grown until growing phases meet each other with vanishing unidentified regions. The method requires a limited number of manual parameters that are easily determined. The developed method is illustrated based on three applications on granular materials, comparing the phase volume fractions obtained by segmentation with macroscopic data. It is demonstrated that the algorithm rapidly converges and fills the image after a few iterations.

Keywords Granular media · Sand–bentonite mixtures · Segmentation · Simultaneous region growing · X-ray tomography

1 Introduction

X-ray computed tomography (X-ray CT) is a powerful non-invasive technique to obtain a three-dimensional representation of objects. From the radiograms of the objects, the computer treatment of the set of images allows obtaining a full three-dimensional gray-level picture representing the X-ray attenuation of the material at the considered location. Used nowadays for a wide variety of applications, this technique was introduced initially for medical imaging [30]. A quite complete review of the possible use of X-ray CT can be found in [33]. The first microscale tomography [X-ray microcomputed tomography (X-ray μCT)] was performed by Elliot and Dover [18], with a voxel resolution of 15 μm.

X-ray CT also made its way to geosciences for which a wide range of issues can be treated. A review can be found in [16, 34, 41]. Tomography carries the main advantage that the microfabric of materials is not disturbed by the observation technique, the method being non-invasive. The tomography applications for porous media are mainly focused on (1) the analysis of porosity and fluid flow [46], (2) the evaluation of densities, water contents and volume fractions in general [2, 51, 60] and (3) the characterization of asphalt and concrete microstructures [57, 66].

M. A. Hashemi (✉) · B. François · T. J. Massart
Building Architecture and Town Planning Department (BATir),
Université Libre de Bruxelles, Avenue F.D. Roosevelt 50,
CP 194/2, 1050 Brussels, Belgium
e-mail: mihashem@ulb.ac.be

B. François
e-mail: bertrand.francois@ulb.ac.be

G. Khaddour · S. Salager
CNRS UMR 5521, 3SR Lab, Grenoble-INP, UJF-Grenoble 1,
38041 Grenoble, France

In addition, in a geomechanical context, tomography can be used to characterize local deformations within a soil sample in a mechanical testing device (see [38] for rock materials and [15, 26, 27] for sandy soils). The technique allows producing full three-dimensional numerical images with details such as the shape of sand particles [65], their spatial distribution and arrangement, as well as the pore size distribution [35]. In [3], triaxial tests on different types of sands were also analyzed in relation with the evolution of the samples fabric to understand the development of shear bands at the microstructural scale. For numerical simulations, tomographic images can be directly translated into models for mechanical analysis, as performed using level-set segmentation in porous media for X-FEM numerical simulations in [37]. Besides X-ray CT scanning, other methods of tomography are currently being considered in geomechanical applications, such as neutron imaging [31], magnetic resonance (mostly for water analysis) [5] and gamma ray computed tomography [48].

In image reconstitution, the main challenge consists of treating 3D tomographic data to distinguish the different phases in the heterogeneous material, based on the voxels' gray values. With the naked eye, it seems possible to distinguish the regions occupied by each phase. However, due to the large number of particles in granular materials, visual intuition is practically not sufficient. The phase segmentation must therefore be automated using computational methods to obtain quantitative results. Numerical criteria must be defined to extract phase boundaries in a fast, easy and systematic procedure. This treatment aiming at the partition of the image into a limited number of entities is called 'image segmentation.' A complete overview of digital image processing is presented in [50]. Many methods have been developed for this purpose such as edge detection [11, 40], split and merge [29], watershed [9], stochastic watershed [4], level set [39, 56], region growing [1, 47] and statistical region merging (SRM) [44]. For the purpose of multiphase (or multilabel) segmentation, some authors use the raw image as a result of an original image behaving as a Gibbs distribution following Bayesian statistics. The retrieval of the original image can be made by simulated annealing [22], by iterated conditional modes [8] or using graph theory through graph cuts [25]. A faster approach has also been developed by [10] in the field of early vision segmentation. Multiphase image segmentation can also be seen as a Potts model. A recent survey on different solving algorithms for this model has been presented in [43]. The use of an appropriate relaxation improves the efficiency of the problem solving such as the convex relaxations presented in [67] or in [49]. Level-set-based techniques have also been adapted to multiphase images [62]. Alternatively, the random walker algorithm can also be used as an efficient method of segmentation for multiphase materials [24]. An optimization, called power watershed, using a combination of the random walker, graph cuts and watershed, has been proposed by [14].

For X-ray tomographic images of geomaterials, these approaches could be used for segmentation. However, the type of image to analyze is quite specific for geomaterials. For such materials made of three (or a limited number of) phases, the image is composed of three (or a limited number of) almost-constant gray levels, homogeneously distributed in a granular way into space. However, the segmentation should face two artifacts: Gaussian noise and partial volume effect (PVE). Consequently, existing segmentation methods, initially disposed for classical photography, are not directly suited for geomaterials. In a way, if the histograms of the different phases are separated, there would be no need of a segmentation method as a simple threshold on the gray levels would be sufficient. On the contrary, if the histograms overlap, the simple thresholding method cannot be selected, except if an edge-preserving filter can be applied to decrease the width of the gray-level distribution of each phase in order to remove the overlapping and retrieving the method of simple thresholding. In this paper, several filters can be taken into account such as median, bilateral [61], morphological [55], anisotropic diffusion [45] and total variation minimization [12]. For comparison purposes, other ways to segment the tomographic image have been added in one validation example of Sect. 5.

Consequently, specific image segmentation techniques have been adapted for granular media. An overview of different image processing methods and an investigation on image enhancement is presented in [32]. Most of the research effort has been devoted to the development of approaches to segment biphasic geomaterials, using watershed [21], gradient masks [54] or a combination of both [59]. An improvement in the watershed method called stochastic watershed [4] was shown to be suitable for granular media [19, 23]. Dual filtering combining two different filters together was used in [42] for two-phase segmentation. In spite of these efforts, research is still ongoing for geomaterials with more than 2 phases. In [36], gradient masks followed by watershed are used to extract 3 phases of building stone samples.

The method presented in this paper is a region-growing type segmentation that allows performing segmentations of three-phase tomographic images of a granular material. Therefore, for granular media, all the grains belong to one phase and are embedded within a matrix consisting of two other phases. The main idea is to use the region-growing method simultaneously for each considered phase. The approach is based on the assumption that the noise is homogeneously distributed in the obtained image. The illustrations of the methodology provided in this paper are

mainly focused on granular soil tomography samples, but it can be extended to other types of heterogeneous geomaterials such as concrete, rock, asphalt and ceramics.

The region-growing method in this paper is inspired from the method as originally detailed in [1]. The difference lies in the definition of seeds and will be explained in Sect. 2. Other region-growing criteria have also been developed afterward. Instead of comparing the mean value of the gray levels of pixels included in each region, Chang and Li [13] developed an analysis of the feature of regions' histogram. Hojjatoleslami and Kitter [28] use as growing criteria, two discontinuity measurements: the average contrast and the peripheral contrast. Wan and Higgins [64] developed a method called symmetric region growing, which solves the problem of seed-order dependency in region growing.

Section 2 will first explain the motivations for the development and the specificities of the proposed approach, as well as the conditions for which the method is effective. The complete procedure will then be detailed in Sect. 3. The efficiency of the methodology will be assessed and illustrated in Sect. 4, based on its applications for three granular materials: a sand–bentonite mixture with voids, an unsaturated spherical glass bead sample and an unsaturated sand. The obtained results will be analyzed and discussed in section in light of multiphase porous medium concepts.

2 Challenges in segmenting granular material images

2.1 Gaussian curve overlapping

In the ideal case, the segmentation of an image into different phases is made through a simple histogram threshold as presented in Fig. 1. Figure 1a represents an image obtained for an inclusion-based system. In Fig. 1b, this image is represented by means of a histogram representing the amount of pixels with respect to their gray value. The dark and light phases are well separated, and two Gaussian curves can be identified by a simple threshold giving a satisfactory result as illustrated in Fig. 1c. However, sometimes, the histogram of different phases can overlap due to the presence of noise. Consequently, a single threshold of the gray value is not sufficient to properly distinguish the different phases. Figure 2a illustrates this overlapping through a grain-scale tomography of a three-phase material (sand–bentonite mixture including also void space). The phases in the image are sand particles (the high peak corresponding to bright gray), bentonite (large Gaussian curve in the middle gray values) and air voids (small step for low gray values). The histogram is such that a simple threshold of the image will attribute a part of the region of each phase mistakenly to other phases.
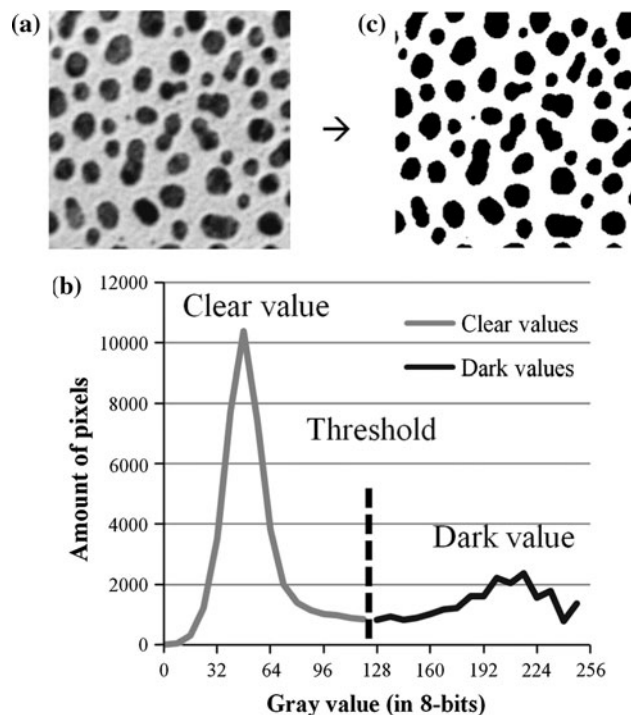

Fig. 1 **a** Image with two distinct *gray values* (from ImageJ): *black dots* and *white background*, **b** simple threshold on the histogram of the image giving and **c** good-quality segmented image
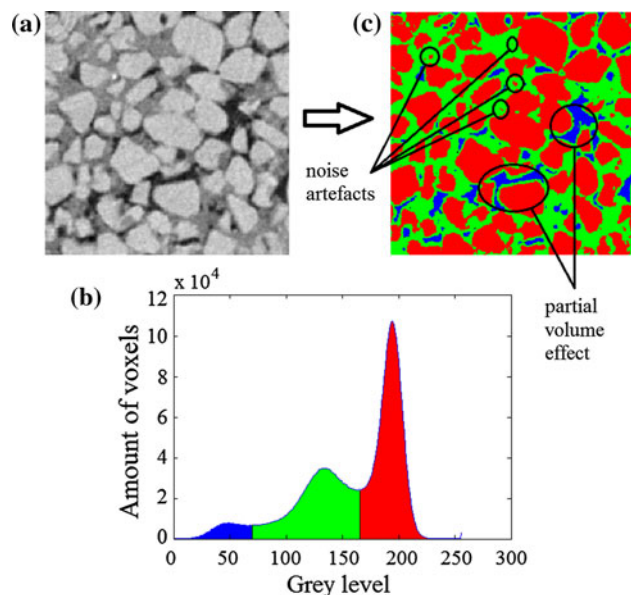

Fig. 2 **a** Microstructure of three-phase material (sand, bentonite and voids), **b** simple threshold on the image and **c** corresponding poor recognition of phases (color figure online)

Conversely, the human eye has the ability to distinguish and to locate properly each phase by accounting for the geometry of the problem. The procedure recognizes that if a voxel is surrounded by other voxels of approximately the

same gray value, it should be considered as belonging to the same phase. This fact is not accounted for when using a simple thresholding approach where voxels are taken individually regardless of the surrounding neighbors. Consequently, a proper thresholding must consider not only the gray intensity of the voxels but also their relative positions. A salient feature of Gaussian noise in images is its homogeneity in space distribution: If for instance the 50 % brightest voxels belonging to one phase are thresholded, the other 50 % remaining voxels have a high probability to be only a few pixels away from the first 50 %. For the application of sand and bentonite mixture, Fig. 3 highlights, on the upper left corner, the 50 % highest gray levels of sand. The corresponding histogram fraction is depicted in red. The procedure of growth consists of taking into account the direct neighbors of the partially thresholded voxels. Since the image is three-dimensional, there are six neighbors next to each voxel considered. In Fig. 3, the six neighbors of the partially thresholded voxels are represented by the dark green fraction of the histogram, which represents the first growth of the partial threshold. These neighbors practically fill the other half of the sand phase. As more neighbors are selected, the sand Gaussian curve is completely filled, but there is then a probability for other phase voxels to be mistakenly selected as belonging to the sand phase.

In Fig. 5a, the partial thresholdings are performed simultaneously on the three phases of the sample of sand–bentonite mixture. Sand, bentonite and macrovoid partial thresholds are, respectively, shown in red, green and blue. The selection made by partial thresholding is
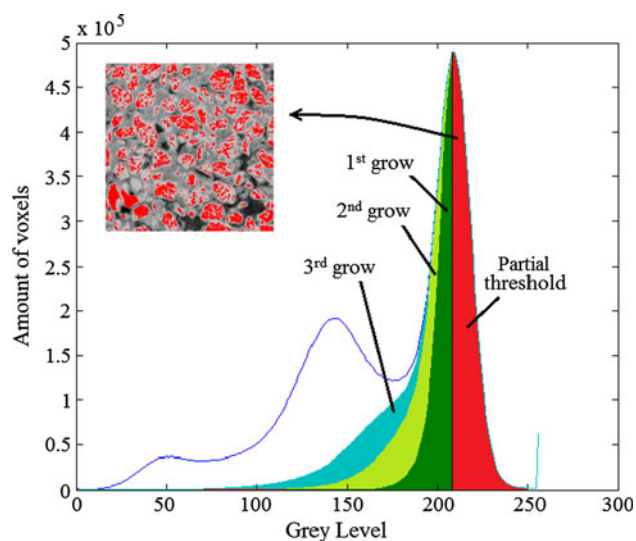

Fig. 4 The use of L_1 distance is justified by the property of region growing
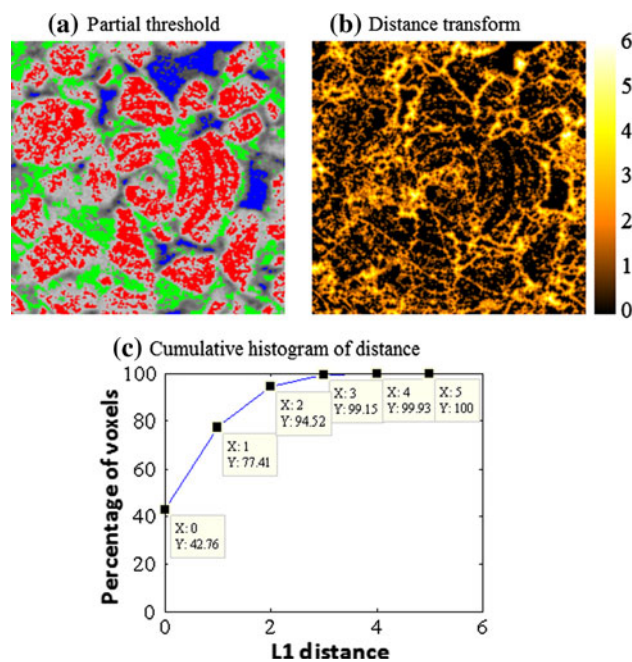
Fig. 5 a Partial thresholding of all three phases simultaneously: sand (*red*), bentonite (*green*) and voids (*blue*) (the PVE—defined in Sect. 2.2—has been removed from the bentonite phase); **b** distance field (with L_1 norm) of the picture **a** representing the distance from the nearest phase selected in the partial threshold; **c** cumulative histogram of distances in (**b**) (color figure online)

homogeneously distributed in each phase. Consequently, each partial threshold will exert a 'barrier' against other phases, preventing them from growing toward its direction. An illustration of how fast this method fills the image is given, for each voxel outside any partial threshold, by its distance from the nearest voxel inside the partial threshold. The proper distance to use for this purpose is the L_1

Fig. 3 Histogram of the neighbors of the partially thresholded voxels of the sand phase represented in the *upper left corner*: after successive growing, the selected voxels fill the other side of the sand's Gaussian curve (color figure online)
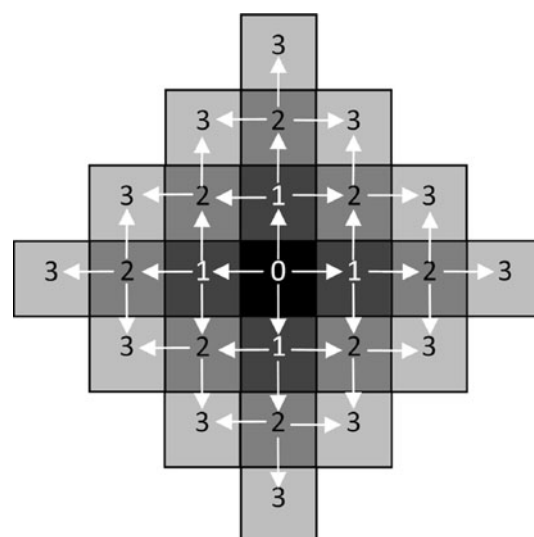
distance because region growing is made by successive dilations of each voxel into its six neighbors. The L_1 distance between two voxels of coordinates $\mathbf{x_1}$ and $\mathbf{x_2}$ is defined by

$$\|\mathbf{x_1} - \mathbf{x_2}\| = |x_1 - x_2| + |y_1 - y_2| + |z_1 - z_2| \qquad (1)$$

where $\mathbf{x_i} = (x_i, y_i, z_i)$ are the 3D coordinates of the voxels. A voxel located at $\mathbf{x_2}$ having a L_1 distance of d from the nearest partial threshold located at $\mathbf{x_1}$ will undergo the region growth after the dth iteration as shown in Fig. 4.

The nearer the voxel outside the partial threshold, the sooner it will be filled by region growing. Figure 5b shows this distance map. Most of the voxels (more than 99 %) outside these partial thresholds are far of 3 voxels or less. To further illustrate this, the cumulative graph shown in Fig. 5c represents the proportion of voxels selected as a function of the distance to the nearest partial threshold. The proportion of voxels in the partial thresholds is around 40 %, the six neighbors (touched by the first iteration) are more than 30 % summing it up to around 77 %. This figure shows how the simultaneous region-growing method can rapidly fill all the space after a few iterations.

The partial thresholding is used to define the seeds of each phase before region growing. In the original methodology presented in [1], seed positions are selected interactively by the user to locate the seeds by hand. When dealing with granular media, it is not possible to use an interactive method because of the number of seeds required. Automated seeding can be made through edge detection [20] or by defining criteria using the neighbors of each pixel [58]. In our case, taking seeds from a gray-level threshold is simple and fast. It is also efficient because the seeds are located homogeneously throughout the phases, thanks to the Gaussian noise.

2.2 Partial volume effect

Another issue of phase recognition is the problem of PVE. In Fig. 1b, gray levels located between the two Gaussian curves are due to PVE as a consequence of the image resolution. This effect appears when two phases in reality are taken into account into one voxel. This voxel is then representative of both phases showing an intermediate gray level corresponding to a balanced average of the gray levels of two distinct objects. The gray value of PVE depends on the percentage of each phase in the voxel. This effect is especially critical for images where three phases have to be considered. Thresholding the image by selecting the middle phase will also select voxels located at the interface between the two others due to PVE. The PVE filtering has the goal to remove the seeds wrongly attributed to the middle phase due to PVE. Available corrections of PVE consist mainly of removing PVE with an image

filter as if it resembled to blur [6, 52]. In the present approach, the problem of PVE is taken into account as a complement to refine the seed definition made by partial thresholding. Since PVE is located at the edges of different phases, the definition of PVE in seeds is made through the use of a variance filtering, but other filters can be used to localize boundaries and possible PVE locations (Laplacian, Sobel, Kirsch, Canny, see [7] for a survey).

3 Enhanced segmentation procedure

Based on the above-mentioned considerations, the full procedure followed for the image segmentation of granular media will now be detailed. This procedure is divided into four steps: (1) partial thresholding, (2) PVE filtering, (3) simultaneous phase growing which constitutes the main step and finally (4) interface filling. This complete procedure will be explained here with illustrations on the sand–bentonite mixture, keeping in mind that it can be applied to any three-phase granular medium.

3.1 Partial thresholding

The first step of this method consists in seeding the regions where each phase is present. This can be done by thresholding the gray values where the Gaussian curves are not overlapping. This preliminary thresholding is performed based on the shape of the gray-level histogram. This partial threshold is crucial for the efficiency of the method. The percentage of selected pixels must be a good compromise. Selecting too few voxels would not allow having a good predictor of the phase organization, while selecting too many could incorporate voxels from another phase. A good compromise consists of selecting the partial thresholds based on the peaks on the histogram of the image. The selection is represented in Fig. 6 that represents the histogram of the sand–bentonite mixture presented in Fig. 2. The thresholds are initially selected as follows. The sand threshold isolates the 50 % upper part of the sand Gaussian curve, and the void threshold isolates the 50 % lower part of the void Gaussian curve. For the bentonite, since this is the intermediate phase, the thresholds are defined to select 25 % dark (left) and 25 % bright (right) pixels starting from the corresponding peak. This is achieved by locating where the Gaussian curve of this phase decreases to 80 % of its peak.

Note that the amount of each phase considered in the partial thresholding may be chosen as a function of the noise present in the image, due to its impact on the amount of overlapping on the Gaussian curves. If the overlapping becomes larger, the procedure shown in Fig. 6 should be replaced by a graphical localization of selected voxels from
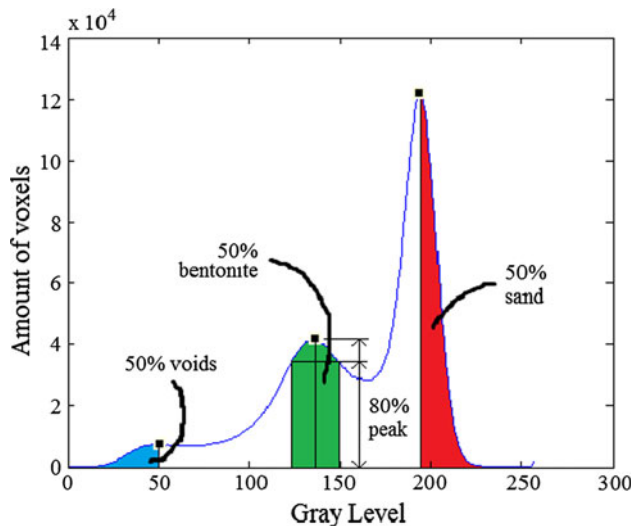
Fig. 6 Procedure to choose the partial thresholds for each phase: lower half for void phase, upper half for sand phase and from the first to the third quartile for the bentonite phase (meaning taking the Gaussian curve until it decreases to 80 % of the peak) (color figure online)

Fig. 7 a Standard deviation increases from clearer to darker. **b** Standard deviation threshold is taken on the inflexion point of the histogram of standard deviations (color figure online)

Fig. 8 Difference between real phase and PVE: In the histogram, real bentonite (*green*) is unimodal, whereas PVE (*red*) is bimodal (void and sand) (color figure online)

successive thresholds. Good partial (initial) thresholding is essential to avoid wrong seeds. Excessive overlapping decreases the chances of finding good thresholds and may result in failure of the proposed method. In this case, a preliminary noise treatment could be recommended in order to obtain histograms with less Gaussian curve overlapping and easier definitions of partial thresholds. The fractions of each phase selected here may appear relatively arbitrary. However, they will be shown to yield good results not only for the sand–bentonite mixture but also for other materials (see Sect. 4). Note, however, that these proportions can be adapted as a function of the tested materials and the shape of the histogram.

Of course, by definition of the X-ray tomography, this method of segmentation is only possible if density contrast between the different phases is sufficient to avoid any overlapping of the peaks of the histogram, which would make partial thresholding impossible.

3.2 Middle-phase PVE filtering

Figure 7 exhibits an example of the middle-phase partial threshold. For a three-phase material (as in the present case), four groups of voxels emerge after partial threshold: the dark phase (B_1), the middle phase (B_2), the bright phase (B_3) and the remaining non-selected voxels (R).

From the partial threshold step, the PVE must be properly identified. It consists of voxels of the group B_2, which have specific properties. The PVE between the lowest gray phase and the highest gray phase gives a gray value in the middle range.
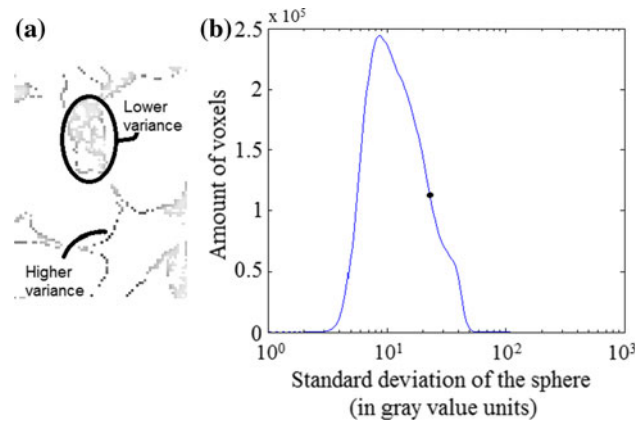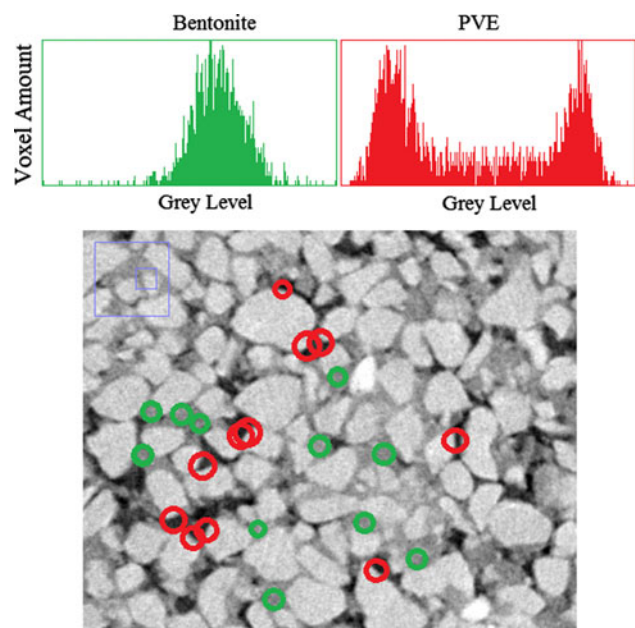
The difference between the gray value of the middle phase and the gray value caused by PVE can be noticed from the surrounding of corresponding voxels. The surrounding of a voxel from the middle phase is composed of voxels having close gray values. A spherical selection around this voxel will result in the histogram in an approximate Gaussian curve centered on the middle-phase gray value (see Fig. 8 in green). Conversely, the surrounding of a voxel from the PVE region mostly contains voxels from both the clear and dark gray phases, which results in the histogram of the voxels selected on the sphere in two Gaussian curves representing dark and clear gray voxels (see Fig. 8 in red). In this paper, an optimal radius of

2 voxels is used for this spherical selection. Choosing a radius of 1 voxel (representing the 6 nearest neighbors) would not give sufficient information for the variance calculation, while a larger radius would not consider the direct neighborhood of the voxel. The standard deviation of the voxels surrounding each voxel in B_2 can be used to separate the real middle-phase voxels from PVE voxels as illustrated in Fig. 7a. Those in B_2 with high standard deviation are then excluded by using a threshold filtering of the standard deviation. Figure 7b shows a histogram of the standard deviations for the bentonite phase. This is related to the voxels in B_2 having close gray values on their neighborhoods. The standard deviation of voxels representing PVE is higher, causing, on the histogram, a small increase in high standard deviation values. The threshold is here taken at the inflexion point on the histogram. In Fig. 9a, the standard deviation filter of all the voxels belonging to B_2 with a gray level representing the standard deviation is represented (as shown in Fig. 7a). The result of the standard deviation threshold is shown in Fig. 9b with the PVE at the top and the filtered middle phase at the bottom. After PVE filtering, voxels considered as PVE are excluded from B_2 and put into R. As can be observed, this adaptation shows a good efficiency by filtering most of the voxels located at the interface between voids and sand particles.

3.3 Simultaneous phase growing

At the beginning of this step, each voxel of the image belongs to one of the four following sets: B_1, B_2, B_3 or the remaining voxels R. The method consists of growing all three phases into R, only in the directions where no other phase is present. The growth stops when all the voxels
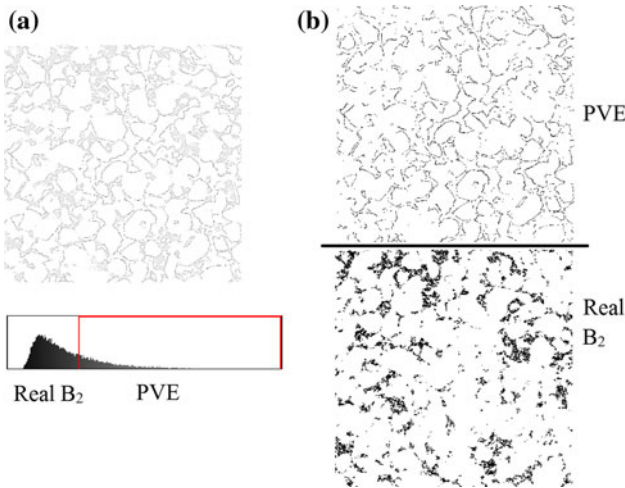
belonging to R have at least two distinct phases as neighbors. At this stage, these remaining voxels represent the interface between different phases. This interface is not assigned to any phase yet because it can belong to one of the neighbor phases without any criterion of choice yet. Figure 10 depicts a Venn diagram of one iteration. Neighbors of phases B_i are called N_i. The voxels selected for growing are called M_i. The rest of the voxels are neighbors of at least two phases and are put in a set called I (as for interface). At the end, the selected sets M_i are added to each phase. The new sets are called B'_i. The sets are defined as follows:

$$M_i = N_i \setminus \underset{i \neq j}{\cup}\left(B_j \cup N_j\right) \tag{2}$$

$$B'_i = B_i \cup M_i \tag{3}$$

$$I = \left(\bigcup N_i\right) \setminus \left(\bigcup B'_i\right) \tag{4}$$

The sets B_i are then replaced by B'_i and the growth continues until all voxels of the set R are either in one of the B_i or in I.

Fig. 9 Thresholding standard deviation for PVE filtering: **a** the set of B_2 with a gray intensity corresponding to the standard deviation and **b** separation of PVE and real B_2 phase by a threshold on the standard deviation (color figure online)
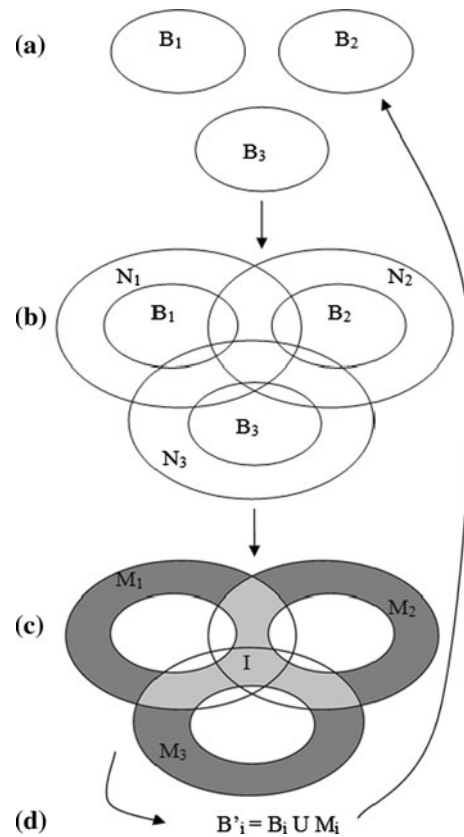
Fig. 10 Venn diagrams showing how growing is made: **a** the initial set of phases; **b** the N_i set represents the neighbors of B_i (intersecting each other); **c** the neighbors added (M_i) are only those who do not intersect with other neighbors; **d** the set M_i is added to B_i and the loop continues

When phases are growing simultaneously, the only criterion to control the growing is the interface set. This means that the first phase that 'reaches' a new voxel incorporates it, and the phases do not 'see' where they grow. Consequently, there is a potential for overgrowing in some areas of the image. This phenomenon may be limited by choosing adequate partial thresholds at the beginning of the process: The initial phases will prevent other phases from growing in their neighborhood. However, it may happen that some areas are not properly seeded for growing, which may result in other phases growing in the area. Consequently, the basic methodology has been improved as follows.

A first improvement is to avoid for each phase to grow in extreme gray values. For each phase, a 'tolerance threshold' is therefore chosen to exclude the gray values where the phase is assumed not to exist. These exclusions can be determined by setting the gray value from which the Gaussian curve of each phase can be neglected.

The existence of PVE must also be considered. After PVE filtering, some voxels (belonging to phases 1 or 3) of phase 2 are not taken into account inside the partial threshold. The tolerance threshold for the phases 1 and 3 has to be large enough to consider these voxels. Consequently, it is recommended to define the tolerance thresholds of phases 1 and 3 as equal. Figure 11 summarizes the choice of both the partial and tolerance thresholds in this procedure.

3.4 Interface filling

At the end of the phase growing step, some of the voxels remain in I. The final step of the procedure is to affect the voxels belonging to the interface to one of the phases. For each voxel inside I, a sphere selects the surrounding voxels. The most present phase inside the sphere will determine the phase segmentation. If two phases are in equal amount in the sphere, the considered voxels remain undecided. This procedure is repeated, and usually after four repetitions, the majority of the voxels have been filled. At the end, the remaining voxels are defined with a simple threshold method and the phases are attributed as a function of the voxels' gray level.

4 Results

As mentioned above, the methodology was developed to trinarize tomographic images of sand–bentonite mixtures treated with lime. However, to further illustrate the flexibility of the method and to provide a quantitative validation, images of two other three-phase granular materials have also been tested. The first is a sample of unsaturated spherical glass beads, and the second is an unsaturated sample of sand.
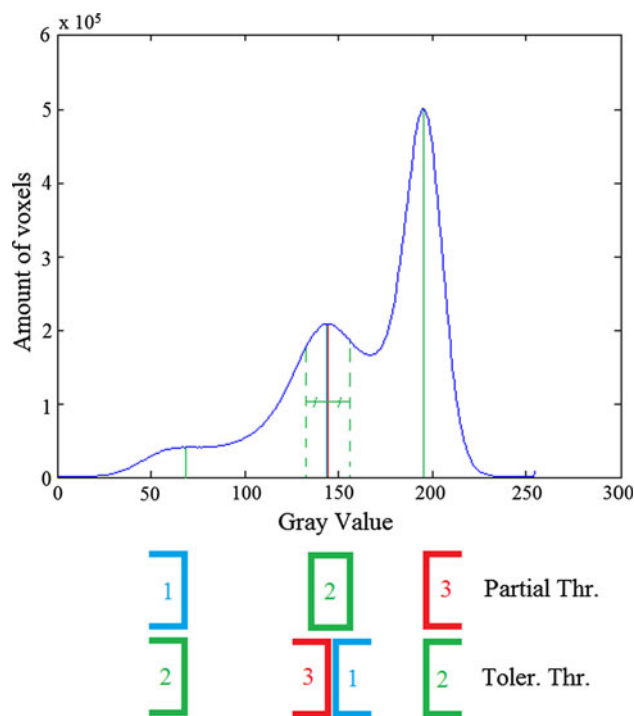

Fig. 11 Procedure for choosing tolerance thresholds from partial thresholds: For phase 2, take the partial thresholds of phases 1 and 3; for phases 1 and 3, take the middle of the partial thresholds of phase 2 (color figure online)

4.1 Sand–bentonite mixture

A sample of mixture of sand and bentonite was analyzed in X-ray CT. The dry mixture was prepared by mixing 20 % bentonite and 80 % sand in mass. Afterward, 1 % of lime was added. The mixture was then mixed by hand until reaching full homogeneity. Finally, 20 % of water content is incorporated and again mixed by hand. It is then put at 20 °C for 24-h mellowing. The sand used is homometric with sizes ranging from 0.15 to 0.35 mm in diameter and $D_{50} = 0.25$ mm. This mixture is then put in a Plexiglas hollow cylinder for X-ray CT. The inner size of the cylinder is of 10 mm diameter and 10 mm height. The tomography shows three main phases: macrovoids, lime–bentonite–water mixture and sand particles. The volume percentage of sand grains can be used to assess the efficiency of the segmentation methodology. The theoretical mass of sand is 72 % of the total mass. Knowing the density of the sample (ρ) = 1.972 g/cm^3 and the specific density of sand itself (ρ_s = 2.648 g/cm^3), the volume proportion of sand is equal to 53.7 %. The resolution of the tomographic images is of 1,500 × 1,500 × 1,500 voxels, and the size of each voxel is around 8 μm. Each voxel is characterized by a gray value stored as a single floating-point number.

Tolerance thresholds have been chosen as follows: Thresholds for the middle phase are determined as the

partial thresholds of both first and third phases, and the tolerance thresholds of the first and third phases are both equal to the mean value of the second-phase partial thresholds. These parameters are illustrated in Figure 11. The main steps of the procedure are illustrated in Fig. 12. The initial grayscale image (Fig. 12a) is initially segmented with partial thresholds (Fig. 12b), the threshold values being taken from histograms (as shown in Fig. 11). Figure 12c is the PVE-filtered image, and the growing evolution is shown in Fig. 12d, e. After phase growing (Fig. 12e), the remaining interface fills 2 % of all the voxels in the image, meaning that phases are already filling most of the image. The final result (Fig. 12f) shows the trinarized image of the interface filling. Counting the number of voxels in each phase, the percentage is shown in Table 1. Taking the fraction of voxels considered as sand, this macroscopic value (51.1 %) is close to the volume fraction computed based on the material preparation data (53.7 %). Figure 13 shows the histogram of each phase after trinarization.
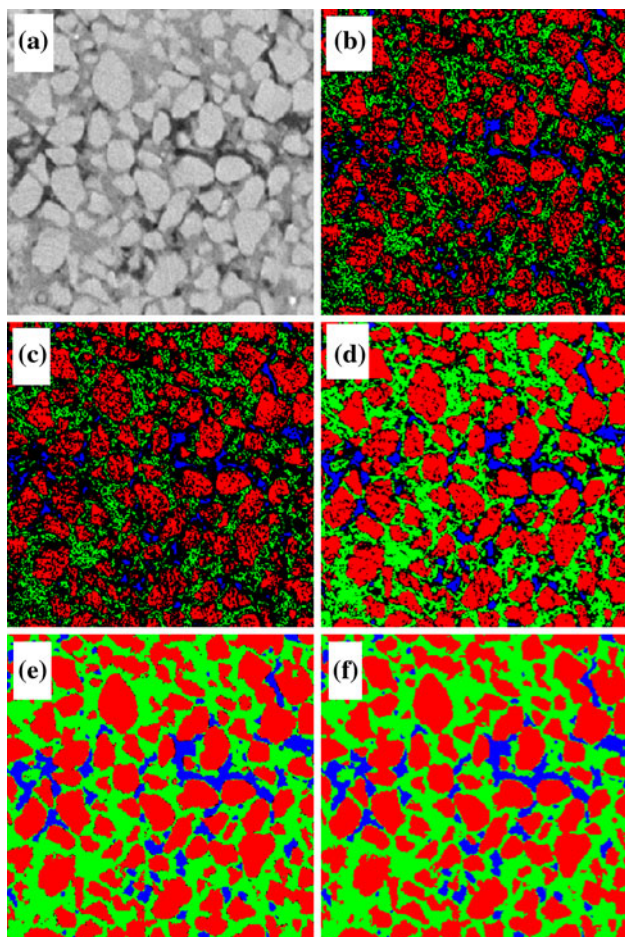

Fig. 12 Evolution of the algorithm on an example of sand–bentonite mixture (color figure online)

Table 1 Final volume fraction of each phase

Phase	Volume percentage
Sand	51.1 (theory: 53.7 %)
Bentonite	38.3
Macrovoids	10.5

4.2 Unsaturated glass beads

A sample of unsaturated spherical glass beads was cylindrically shaped (10×10 mm) with a total volume of 0.785 cm^3. The grain size ranges from 0.665 to 0.735 mm in diameter and $D_{50} = 0.7$ mm. The beads' density is about $\rho_s = 2.5$ g/cm^3. The sample was air-pluviated in a polycarbonate cell. The dry mass of the sample was 1.28 g, which leads to a porosity of 34.7 %. The sample was then analyzed through X-ray CT, and the trinarization of the extracted images is made with a degree of saturation of 16 %, which corresponds to a calculated volume of water of 0.044 ml.

In these results, it has been noticed that the image suffers from beam-hardening effect, making the image borders brighter than the center. Since this trinarization method is strongly based on the values of partial and tolerance thresholds, it is not possible to make a trinarization of the whole image. The trinarization shown for this sample is therefore shown only for the core of the sample. The size of the image is $400 \times 400 \times 400$ voxels. The result is shown in Fig. 16b next to the original image Fig. 16a. Notice that the size of the circles representing the glass beads in the 2D image does not represent the spherical grain size because it shows a cut, which shows glass beads cut at different depths.

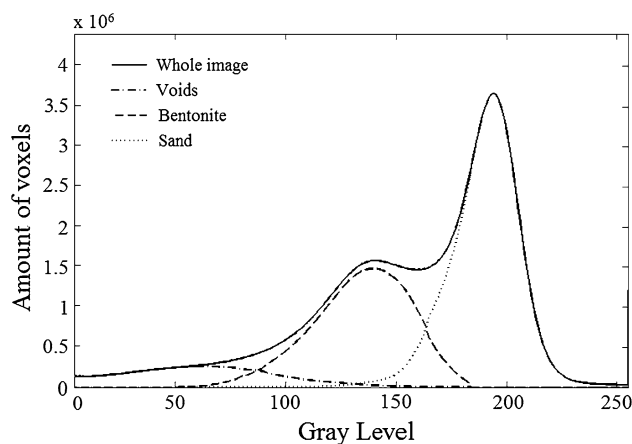The degree of saturation of the sample cannot be compared with the global value because water formations

Fig. 13 Histogram of the trinarized image with the extracted Gaussian curves of each phase
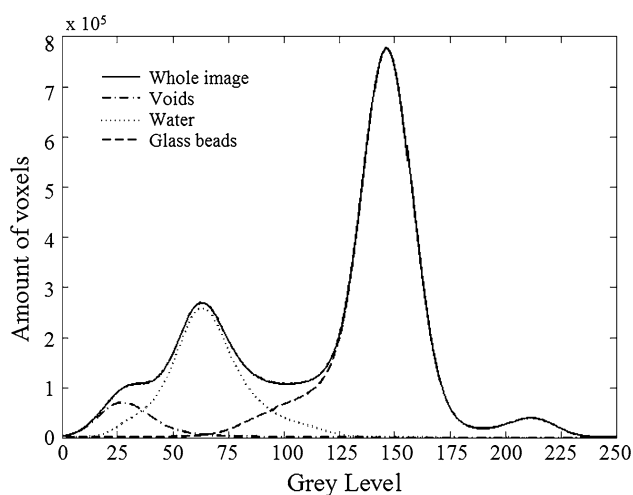
Fig. 14 Histograms of each phase: voids, water and glass beads surrounded by the whole-image histogram

around the glass beads behave as clumps on different locations. The evaluation of the degree of saturation therefore cannot be representative because the segmentation was only performed at the core of the tomographic image. The porosity, however, is homogeneous, and its value (i.e., proportion of voxels labeled as void and water phase) has been determined to be equal to 30.9 %. From a visual point of view, the spherical shape of the beads is very well reproduced by the trinarization procedure. The histogram of the image and the histogram of each phase are shown in Fig. 14. It is shown that the histogram of water does not fill completely the whole-image histogram at its peak. A small fraction of these pixels is considered as either voids or glass beads due to PVE.

4.2.1 Analysis of sphericity

A methodology to analyze the sphericity of glass beads has been considered for the validation of the proposed segmentation procedure. The analysis of the sphericity indeed gives more precise information about the local precision of the image segmentation. The segmented image of the glass beads was analyzed, and the beads have been separated from each other using the Avizo software [63]. Glass beads properly separated by the Avizo software have been
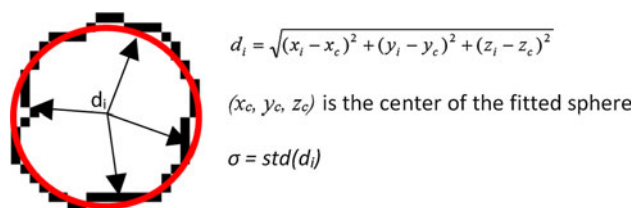

$$d_i = \sqrt{(x_i - x_c)^2 + (y_i - y_c)^2 + (z_i - z_c)^2}$$

(x_c, y_c, z_c) is the center of the fitted sphere

$$\sigma = std(d_i)$$

Fig. 15 Calculation of the accuracy of the segmentation using the deviation of the segmented glass beads with the perfectly fitted sphere (color figure online)
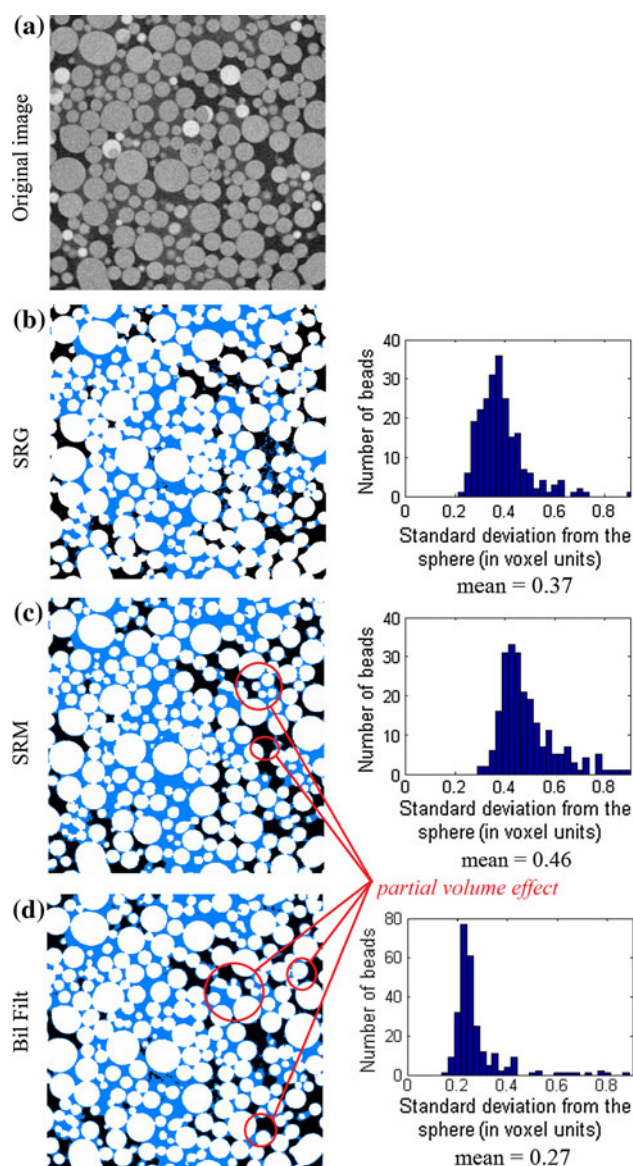

Fig. 16 Result of the trinarization on unsaturated glass beads with sphericity analysis: **a** the original image in *gray* level, **b** the trinarization result (simultaneous region growing), **c** statistical region merging and **d** simple threshold after bilateral filtering. SRM shows higher deviation, but bilateral filter shows lower; however, both do not take PVE filtering into account (color figure online)

extracted and fitted with a spherical model giving the location of the center and its radius according to the procedure described in [17]. The deviation of the glass bead from the sphere has been defined as the standard deviation of the distance between all the voxels of its boundary and the center of the sphere (as the equivalent to the correlation coefficient for the linear regression model). An illustration (in 2D, for the clarity of the image) is given in Fig. 15. The statistical data show a standard deviation of 0.37vx, meaning that for <1 % of the glass beads, boundary voxels are ±1vx outside the perfect sphere. The histogram of the standard

deviation distribution is shown in Fig. 16. The sphericity of glass beads, defined as the ratio of the surface of the glass bead to the surface of the sphere having the same volume as the glass bead, was also calculated according to

$$\Psi = \frac{A}{\pi^{1/3}(6V)^{2/3}} \tag{5}$$

with Ψ being the sphericity, A being the surface of the glass bead and V being its volume. The sphericity of the perfect sphere in this definition is equal to 1, and other geometries have a sphericity higher than 1. In Fig. 17, the number of segmented glass beads is represented as a function of their sphericity. Some of the glass beads have not been properly separated by the software Avizo, showing high sphericity values in the histogram. Also, some beads were not perfectly spherical (but rather ovoidal), which could induce natural sphericity larger than one, independently from the segmentation methods. The mean sphericity (of correctly separated glass beads) given by the segmentation is 1.08, which shows that the local spherical shape of the beads is properly detected by the segmentation procedure.

4.2.2 Comparison with other segmentation techniques

A comparison is given between the proposed trinarization program and two other segmentation methods. The first is the SRM [44] (Fig. 16c), and the second is a simple threshold achieved after noise filtering from bilateral filter (BF) [61] (Fig. 16d). Both segmentations have been performed with the software Fiji [53]. The comparison shows quite similar results between the different methods.

The SRM is performed with the parameter $Q = 25$ (high enough) defining the number of regions accounted (taking $Q = 3$ did not give satisfactory results). Afterward, a manual regrouping is made to merge the 25 regions into 3
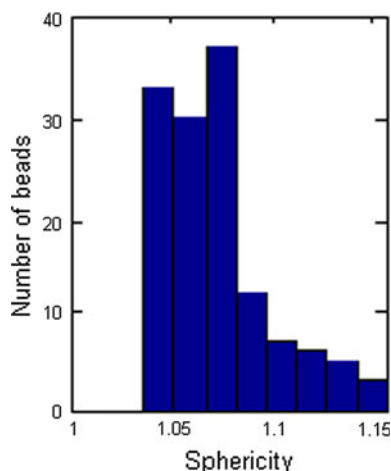

Fig. 17 Histogram of the sphericity calculated for glass beads (color figure online)

corresponding to the 3 phases. Results show no sign of noise artifact, but the PVE is, however, still present.

The bilateral filtering is performed with a spatial radius of 5 voxels and a range radius of 50 gray value units. Once the image is filtered, the segmentation is made by gray-level threshold. The threshold separating glass beads from water and air is tuned, thanks to the a priori knowledge of the porosity of the sample. The threshold separating water and air is defined as the gray value that shows the minimum value between the Gaussian curves of both phases. Results in the image still show some noise artifact. This is due to the Gaussian overlapping still present in the histogram. When thresholding the water phase, PVE is also taken into account and has not been removed.

Table 2 shows the values of the degree of saturation and porosity for the three methods. The degree of saturation (S_r) is equal to the ratio of the volume of water to the sum of the volumes of water and air. The porosity is equal to the ratio of the sum of the volume of water and air to the total volume. The porosity (n) given by bilateral filtering is close to the real value because the simple threshold was defined from the a priori knowledge of the real value. The saturation is higher for the two other methods because it does not take PVE into account.

In addition to the visual comparison, the analysis of the deviation from sphericity was carried out in the SRM segmentation and the bilateral filtering. The results are illustrated in Fig. 16 (right column). The SRM segmentation shows a deviation of 0.46, higher than the segmentation presented in this paper. On the contrary, the bilateral filtering shows a lower deviation of 0.27. This seems lower, but the threshold separating glass beads from the water and air has been tuned to correspond to the target porosity. It may explain that the results are artificially better. Also, the sphericity criterion only checks the segmentation efficiency on the glass beads, which is in favor of this simple threshold because the limit between Gaussian curves of solid and water is well identified. Segmentation made by simple threshold could not segment so properly air and water because the Gaussian curve of air and water phases, although narrower than in the original image, still overlaps. Finally, both SRM and BF segmentations do not take PVE into account.

Table 2 Comparison of volume fractions with different methods

	Reality (%)	Simultaneous region growing (%)	Bilateral filter	Statistical region merging (%)
S_r	–	60.7	64.5 % (min between Gaussian curves of air and water)	63.5
n	34.7	30.9	(34.3 %) (artificially tuned)	36.5

4.3 Unsaturated sand

The sand used for this illustration is the Hostun sand. Its chemical components contain a high amount of siliceous material ($SiO_2 > 98$ %). The grain shape is ranging from angular to subangular. The Hostun sand grain density is $\rho_s = 2.65$ g/cm^3. The grain size varies from 0.1 to 1 mm in diameter and $D_{50} = 0.32$ mm. The dry mass of the sample was 1.24 g.

Hostun sand samples were water-pluviated, and suction was controlled through the experiment, which started from the saturated case, with a gradual increase in suction, until ending up with the dry case [51]. The analyzed image presents a Hostun sand sample under a suction of 2 kPa. Figure 18 shows a cut of the original gray level in Fig. 18a and the resulting trinarization in Fig. 18b. The histogram of the phases (Fig. 19) gives satisfactory results. In this case, the Gaussian curve of the Hostun sand phase is well separated from the other phases. Consequently, sand particles have been selected by a simple threshold and are not included in the region-growing process. This is made possible through the use of identical partial and tolerance thresholds for the sand phase. On the contrary, the gray levels of air and water phases show an overlapping, which occurs mainly for intermediate gray levels (between 100 and 150 on the x-axis of Fig. 19) where voids, water and PVE zone coexist. In particular, PVE plays an important role for those levels of gray because they must be redistributed between the different phases. This explains the apparent continuity in gray level between water and sand particles. The presence of sand phase in gray levels lower than tolerance threshold is due to the interface filling. After the region-growing step, some voxels are located in the group *I*. They are not labeled yet. They can still be selected as sand phase during the interface filling step. Finally, the curves of air and water phases show a successful segmentation of their overlapping in the key region of intermediate gray levels.
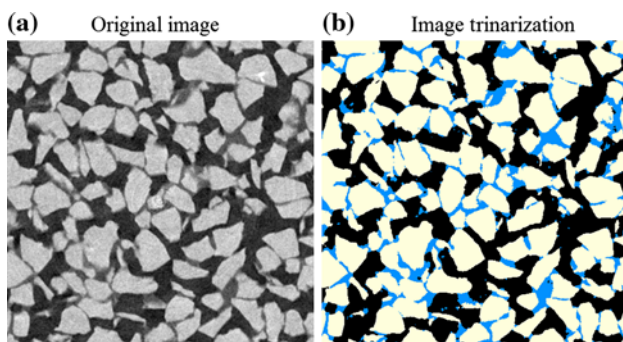

Fig. 18 Result of the trinarization on unsaturated sand: **a** the original image in *gray* level and **b** the trinarization result (color figure online)
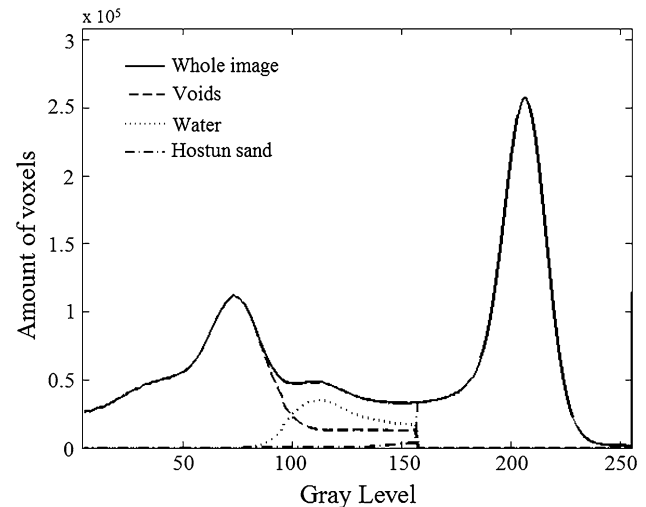

Fig. 19 Histograms of each phase: voids, water and Hostun sand surrounded by the whole-image histogram

5 Discussion

5.1 Parameter tuning

The proposed methodology involves some parameters potentially affecting its efficiency. The influence of these
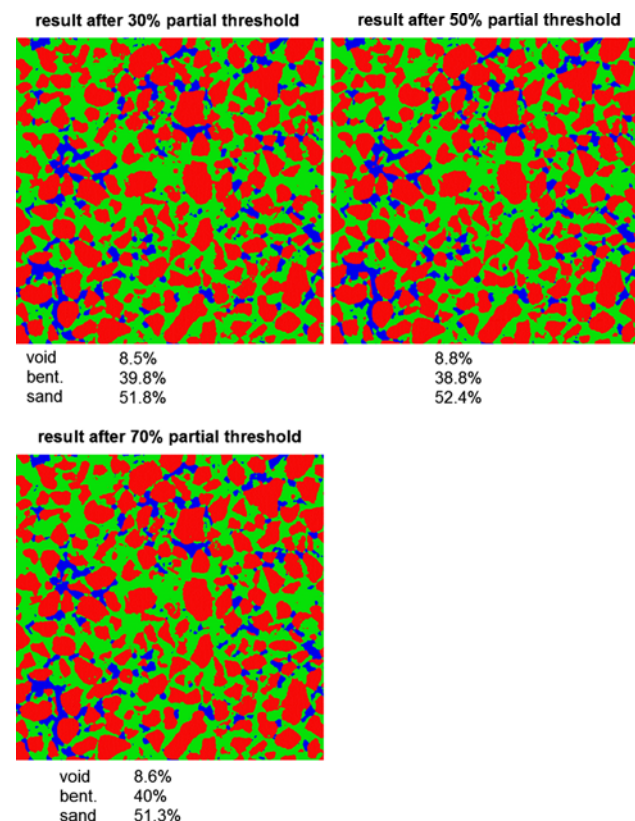

Fig. 20 Choosing as initial partial threshold 30, 50 or 70 % of the whole image does not give a significant change in the results (color figure online)
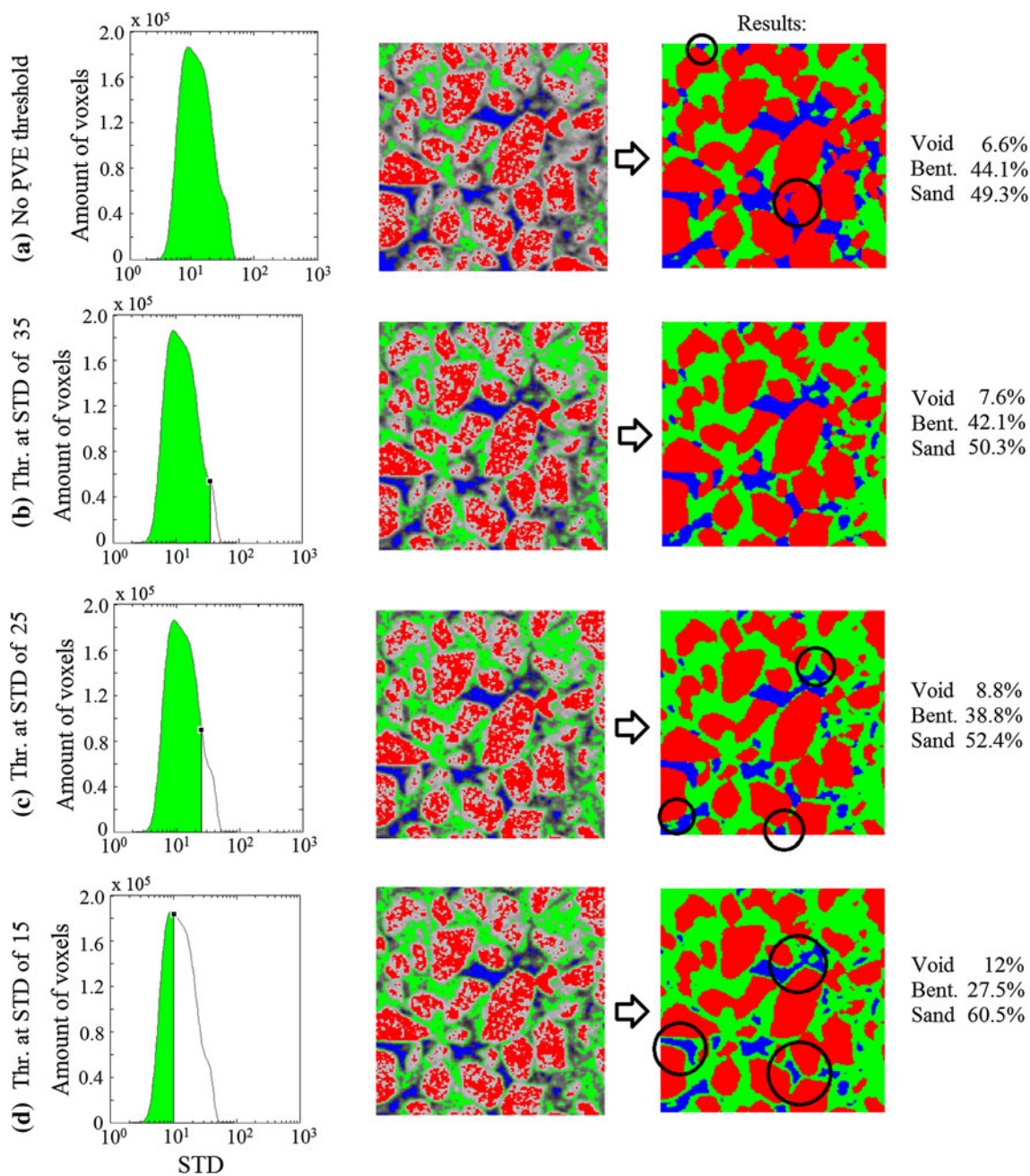
Fig. 21 From **a–d**: thresholding the standard deviation (STD) with lower and lower values. The volume fraction in the results highly depends on the value of the threshold (color figure online)

manual parameters is now briefly discussed based on the sand–bentonite mixture sample. In the procedure, four manual parameters are used:

- 1 parameter for the partial threshold of each phase,
- 1 parameter for the standard deviation threshold regarding the middle-phase PVE filtering.

The determination of the first three parameters was already discussed at the end of Sect. 3.1, where a fraction of 50 % of each phase was chosen as partial thresholds. To

further assess the effect of this choice, Fig. 20 demonstrates that a change (even important) in the partial threshold selection does not give any noticeable influence on the obtained trinarized result, excepted in the image with 70 % of partial threshold where small inclusions of phases can, however, be seen as a result of Gaussian curve overlapping. If a too wide partial threshold is taken, the risk of considering other phases within this partial threshold is increased.

The results in Fig. 20 were all obtained with a standard deviation threshold on the PVE of 25, with the images in

gray level with values ranging from 0 to 255. The effect of variation of this PVE threshold on the standard deviation is illustrated in Fig. 21. Using a lower threshold will lower the amount of seeded middle phase. This results in a lower amount of phase 2, when the threshold decreases.

A too high threshold (see Fig. 21b) will not remove PVE completely. A too low threshold (see Fig. 21d) allows other phases to grow into the middle phase. The reason for the PVE filtering being difficult to deal with is that the values of the PVE standard deviations are overlapping with the real middle-phase standard deviations. The best criterion is thus to select low values of standard deviation to remove most of the PVE. This will also remove a part of the middle phase, but it will be recovered during the region-growing step. The volume fraction of the middle-phase partial threshold will be significantly lower than the volume fraction of the other partial thresholds. Consequently, a partial solution is to account for a more important volume fraction of the middle phase during partial thresholding and remove its excess in the PVE filtering.

5.2 Filtering before segmentation

A comparison is now performed between the segmentation of the original image of sand and bentonite mixture and the segmentation of the same image with a BF previously applied. The filter has been applied by the software Fiji with the parameters with a spatial radius of 3 and a range radius of 50. The results (Fig. 22) show a very light
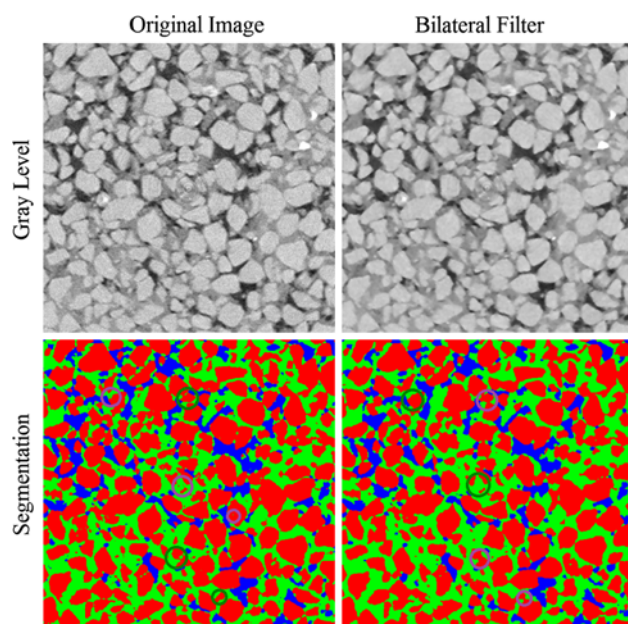

Fig. 22 Comparison between segmentation of an original sand–bentonite mixture image and the same image filtered with a bilateral filter. *Green circles* on the original image show that sharp edges are preserved and in the filtered image that some artifacts are removed (color figure online)

positive effect of the filter that allows removing some artifacts in the segmentation after filtering (see green circles in Fig. 22). In particular, the limit between phases is slightly smoother when it has been preliminary treated with a filter. However, the filter may have a negative influence on the segmentation in the point contacts between sand particles. The smoothing induced by the filter increases the interface curvature and so enlarges artificially the contact between particles (see purple circles in Fig. 22).

6 Conclusions

In this contribution, a new segmentation methodology is presented, allowing us to recognize three-phase material in a 3D X-ray tomographic image. The method uses simultaneous region growing as an improvement in classical region-growing principles. It consists of using the region-growing method simultaneously for the three phases. Each phase stops expanding in directions where other phases are already present. Consequently, the region growing of each phase is controlled spatially by other phases' region growing. This process, however, requires two pretreatments before being initiated. The seeding of each of the three phases from which the growing will occur is first obtained from partial thresholding. Then, the removal of PVE from the seeding of the middle phase is performed. The developed method was shown to yield very good results, provided that the three phases have a good density contrast, allowing the preliminary identification of three distinct phases in the gray-level image. It was demonstrated that the arbitrary choice of the proportion of seeding does not have a significant influence on the result as long as partial thresholding is achieved to select the same proportion of voxels with respect to the total number of voxels in each phase. For example, a seeding of 50 % should consider selecting 50 % of voids, 50 % of bentonite and 50 % of sand as partial thresholds (after PVE filtering). This method is shown to converge quickly after a few iterations (corresponding to successive growing steps). Also, the results match with reality from a qualitative and quantitative point of view: The volume fraction of sand in the sand–bentonite mixture calculated with the region-growing method is close to the experimental macroscopic value. Comparison of this new segmentation method with two other existing and freely available segmentation methods shows that the three techniques provide relatively similar results from a qualitative and quantitative point of view. Nevertheless, the main advantage of this new method is that it can manage to provide segmentation for three-phase images (that can be, as a perspective, extended to the multiphase problem) and treat the issue of PVE in efficient way fully integrated in the methodology.

In some situations, when the low signal-to-noise ratio alters the identification of the peak of Gaussian curve corresponding to each phase, it can be of interest to apply a filter as a pretreatment of the image that could allow to improve the initial seeding of each phase. So, this filter could be a good complement that may improve the efficiency of the method. However, it should be noticed that filtering can affect the geometry such as blunting sharp edges and increases contact surface between particles.

As a perspective, the method can be extended to more than three phases. Adding more phases would imply the use of the PVE filtering on more than one middle phase, the rest of the procedure remaining unchanged.

Also, the idea could be adapted with other methods of image segmentation than region growing such as level-set-based methods [37].

References

1. Adams R, Bischof L (1994) Seeded region growing. IEEE Trans Pattern Anal Mach Intell 16(6):641–647
2. Anderson SH, Gantzer CJ, Boone JM (1988) Rapid non destructive bulk density and soil water content determination by computer tomography. Soil Sci Soc Am J 52:35–40
3. Ando E, Hall SA, Viggiani G, Desrues J, Bésuelle (2012) Grain-scale experimental investigation of localised deformation in sand: a discrete particle tracking approach. Acta Geotech 7(1):1–13
4. Angulo J, Jeulin D (2007) Stochastic watershed segmentation. In: international symposium on mathematical morphology. pp 265–276
5. Asseng S, Aylmore LAG, MacFall JS, Hopmans JW, Gregory PJ (2000) Computer-assisted tomography and magnetic resonance imaging. In: Smith AL (ed) Root methods: a handbook. Springer, Berlin
6. Aston JAD (2002) Cunningham VJ, Asselin M-C, Hammers A, Evans AC, Gunn RN Positron emission tomography partial volume correction: estimation and algorithms. J Cereb Blood Flow Metab 22(8):1019–1034
7. Basu M (2002) Gaussian-based edge-detection methods—a survey. IEEE Trans Syst Man Cybern 32:252–260
8. Besag J (1986) On the statistical analysis of dirty pictures. J R Stat Soc Ser B Methodol 48(3):259–302
9. Beucher S, Meyer F (1993) The morphological approach to segmentation: the watershed transformation. In: Dougherty ER (ed) Mathematical morphology in image processing. Marcel Dekker INC, New York, pp 433–481
10. Boykov Y, Veksler O, Zabih R (2001) Fast approximate energy minimization via graph cuts. IEEE Trans Pattern Anal Mach Intell 23(11):1222–1239
11. Canny J (1986) A computational approach to edge detection. IEEE Trans Pattern Anal Mach Intell 8(6):679–698
12. Chambolle A (2004) An algorithm for total variation minimization and applications. J Math Imaging Vis 20(1–2):89–97
13. Chang YL, Li X (1994) Adaptive image region-growing. IEEE Trans Image Process 3(6):868872
14. Couprie C, Grady L, Najman L, Talbot H (2011) Power watershed: A unifying graph-based optimization framework. IEEE Trans Pattern Anal Mach Intell 33(7):1384–1399
15. Desrues J, Chambon R, Mokni M, Mazerolle F (1996) Void ratio evaluation inside shear bands in triaxial sand specimens studied by computer tomography. Géotechnique 46(3):1–18
16. Desrues J, Viggiani G, Besuelle P (2006) Advances in X-ray tomography for geomaterials. iSTE
17. Eberly D (1999) Least squares fitting of data. Geometric Tools, LLC. http://www.geometrictools.com
18. Elliot JC, Dover SD (1982) X-ray microtomography. J Microsc 126(2):211–213
19. Faessel M, Jeulin D (2009) Segmentation of 3d microtomographic images of granular materials with the stochastic watershed. J Microsc 239:17–31
20. Fan J, Zeng G, Body M, Hacid MS (2005) Seeded region growing: an extensive and comparative study. Pattern Recognit Lett 26:1139–1156
21. Fonseca J, O'Sullivan C, Coop MR (2009) Image segmentation techniques for granular materials. AIP Conf Proc 1145(1):223–226
22. Geman S, Geman D (1984) Stochastic relaxation, gibbs distributions, and the bayesian restoration of images. IEEE Trans Pattern Anal Mach Intell 6(6):721–741
23. Gilibert L, Jeulin D (2011) Stochastic multiscale segmentation constrained by image content. In: ISMM'11 Proceedings of the 10th international conference on Mathematical morphology and its applications to image and signal processing. Verbania-Intra, Italy, pp 132–142
24. Grady Leo (2006) Random walks for image segmentation. IEEE Trans Pattern Anal Mach Intell 28(11):1768–1783
25. Greig DM, Porteous BT, Seheult AH (1989) Exact maximum a posteriori estimation for binary images. J R Stat Soc Ser B 51:271–279
26. Hall SA, Bornert M, Desrues J, Pannier Y, Lenoir N, Viggiani G, Bésuelle P (2010) Discrete and continuum analysis of localised deformation in sand using X-ray ct μct and volumetric data image correlation. Géotechnique 60(5):315–322
27. Higo Y, Oka F, Kimoto S, Sanagawa T, Matsushima Y (2011) Study of strain localization and microstructural changes in partially saturated sand during triaxial tests using microfocus X-ray ct. Soils Found Jpn Geotech Soc 51(1):95–111
28. Hojjatoleslami SA, Kittler J (1998) Region growing: a new approach. IEEE Trans Image Process 7(7):10791084
29. Horowitz SL, Pavlidis T (1974) Picture segmentation by a directed split-and-merge procedure. In: Proceedings of the 2nd international joint conference on pattern recognition, Copenhagen, Denmark, pp 424–433
30. Hounsfield GN (1972) Apparatus for examining a body by radiation such as X or gamma radiation. The Patent Office, Patent Specification 1283915, London
31. Kaestner A, Hassanein R, Vontobel P, Lehmann P, Schaap J, Lehmann E, Fluehler H (2007) Mapping the 3d dynamics in heterogeneous sands using thermal neutrons. Chem Eng J 130(2–3):79–85
32. Kaestner A, Lehmann E, Stampanoni M (2008) Imaging and image processing in porous media research. Adv Water Resour 31:1174–1187
33. Kalender WA (2006) X-ray computed tomography. Inst phys publ Phys Med Biol 51:R29–R43
34. Ketcham RA, Carlson WD (2011) Acquisition, optimization and interpretation of X-ray computed tomographic imagery: applications to geosciences. Comput Geosci 27:381–400

35. Koliji A, Vulliet L, Laloui L (2010) Structural characterization of unsaturated aggregated soil. Can Geotech J 47:297–311

36. Le Trong E, Rozenbaum O, Rouet JL, Bruand A (2008) A methodology to segment X-ray tomographic images of multiphase porous media: application to building stones. HAL—CCSD

37. Legrain G, Cartraud P, Perreard I, Moës N (2011) An X-FEM and level set computational approach for image-based modelling: Application to homogenization. Int J Numer Methods Eng 86(7):915–934

38. Lenoir N, Bornert M, Desrues J, Bésuelle P, Viggiani G (2007) Volumetric digital image correlation applied to X-ray microtomography images from triaxial compression tests on argillaceous rocks. Strain Int J Exp Mech 43(3):193–205

39. Malladi R, Sethian JA, Vermuri BC (1993) A topology independent shape modeling scheme. In: Proceedings of SPIE conference on geometric methods in computer vision II, volume 2031. San Diego, CA, pp 246–258

40. Marr D, Hildreth E (1980) Theory of edge detection. Proc R Soc Lond Ser B Biol Sci 207:187–217

41. Mees F, Swennen R, Van Geet M, Jacobs P (2003) Applications of X-ray computed tomography in the geosciences. Geol Soc Lond Special Publ 215:1–6

42. Müter D, Pedersen S, Feidenhans'l R, Sørensen HO, Stipp SLS (2012) Improved segmentation of X-ray tomography data from porous rocks using a dual filtering approach. Comput Geosci 49:131–139

43. Nieuwenhuis C, Töppe E, Cremers D (2013) A survey and comparison of discrete and continuous multi-label optimization approaches for the Potts model. Int J Comput Vis 104(3):223–240

44. Nock R, Nielsen F (2004) Statistical region merging. IEEE Trans Pattern Anal Mach Intell 26(11):1452–1458

45. Perona P (1990) Scale-space and edge detection using anisotropic diffusion. IEEE Trans Pattern Anal Mach Intell 12(7):629–639

46. Peth S (2010) Synchrotron-based techniques in soils and sediments, volume 34, chapter 3. Elsevier, Amsterdam, pp 73–101

47. Phan DL, Xu C, Price J (2000) A survey of current methods in medical image segmentation. Annu Rev Biomed Eng 2:315–338

48. Pires LF, Robson CJA, Correchel V, Bacchi OOS, Reichardt K, Camponez do Brasil RP (2004) The use of gamma ray computed tomography to investigate soil compaction due to core sampling devices. Braz J Phys 34(3a):728–731

49. Pock T, Chambolle A, Cremers D, Bischof H (2009) A convex relaxation approach for computing minimal partitions. In: Computer vision and pattern recognition, 2009. CVPR 2009. IEEE Conference on IEEE, pp 810–817

50. Pratt WK (2007) Digital image processing. Wiley, Hoboken

51. Riedel I, Ando E, Salager S, Bésuelle P, Viggiani G (2012) Water retention behaviour explored by X-ray CT analysis. In: Proceedings of 2nd European Conference on Unsaturated Soils

52. Rousset OG, Zaidi H (2006) Correction for partial volume effects in emission tomography, chapter 7. Springer, Berlin, pp 236–271

53. Schindelin J (2012) Arganda-Carreras I, Frise E, Kaynig V, Longair M, Pietzsch T, Preibisch S, Rueden C, Saalfeld S, Schmid B, Tinevez JY, White DJ, Hartenstein V, Eliceiri K, Tomancak P, Cardona A Fiji: an open-source platform for biological-image analysis. Nat Methods 9:676–682

54. Schlüter S, Weller U, Vogel HJ (2010) Segmentation of X-ray microtomography images of soil using gradient masks. Comput Geosci 36:1246–1251

55. Serra J (1982) Image analysis and mathematical morphology. Academic Press Inc., Orlando

56. Sethian A (1999) Level set methods and fast marching methods: evolving interfaces in geometry, fluid mechanics, computer vision and materials sciences. Cambridge University Press, Cambridge, UK

57. Shashiidar N (1999) X-ray tomography of asphalt concrete. Transp Res Rec 78(1681):186–191

58. Shih FY, Cheng S (2005) Automatic seeded region growing for color image segmentation. Image Vis Comput 23(10):877–886

59. Tariel V, Jeulin D, Fanget A, Contesse G (2008) 3d Multi-scale segmentation of granular materials. Image Anal Stereol 27:23–28

60. Taud H, Martinez-Angeles R, Parrot JF, Hernandez-Escobedo L (2005) Porosity estimation method by X-ray computed tomography. J Pet Sci Eng 47(3–4):209–217

61. Tomasi C, Manduchi R (1998) Bilateral filtering for gray and color images. In: Proceedings of the IEEE international conference on computer vision

62. Vese LA, Chan TF (2002) A multiphase level set framework for image segmentation using the Mumford and Shah model. Int J Comput Vis 50(3):271–293

63. Visualization Sciences Group (VSG). http://www.vsg3d.com/sites/default/files/AvizoRefGuide.pdf. Avizo 7 ©

64. Wan SY, Higgins WE (2003) Symmetric region growing. IEEE Trans Image Process 12(9):10071015

65. Wand LB, Park JY, Fu Y (2007) Representation of real particles for DEM simulation using X-ray tomography. Constr Build Mater 21:338–346

66. Wang L, Paul HS, Harman T, D'Angelo J (2004) Characterization of aggregates and asphalt concrete using X-ray computerized tomography—A state of the art report (with discussion). J Assoc Asph Paving Technol 73:467–500

67. Zach C, Gallup D, Frahm JM, Niethammer M (2008) Fast global labeling for real-time stereo using multiple plane sweeps. In: Vision, modeling and visualization workshop. Universitat Konstanz, Konstanz, pp 243–252